Landslide-lake outburst floods accelerate downstream hillslope slippage

Wentao Yang[1], Jian Fang[2], Jing Liu-Zeng[3]

[1]Three-gorges Reservoir Area (Chongqing) Forest Ecosystem Research Station, School of Soil and Water Conservation, Beijing Forestry University, Beijing, 100083, China
[2]College of Urban and Environmental Sciences, Central China Normal University, Wuhan, 430079, China
[3]Institute of Surface-Earth System Science, Tianjin University, Tianjin, 300072, China

Correspondence to: Wentao Yang (yang_wentao@bjfu.edu.cn)

Abstract. The Jinsha River, carving a 2-4 km deep gorge, is one of the largest SE Asian rivers. Two successive landslide-lake outburst floods (LLFs) occurred after the 2018 Baige landslides along the river. Using Sentinel-2 images, we examined the LLFs' impacts on downstream river channel and adjacent hillslopes over a 100 km distance. The floods increased the width of the active river channel by 54%. Subsequently, major landslides persisted for 15 months in at least nine locations for displacements > 2m. Among them, three moving hillslopes, ~80 km downstream from the Baige landslides, slumped more than 10 m one year after the floods. Extensive undercuts by the floods probably removed hillslope buttresses and triggered deformation response, suggesting a strong and dynamic channel-hillslope coupling. Our findings indicate that infrequent catastrophic outburst flooding plays an important role in landscape evolution. Persistent post-flood hillslope movement should be considered in disaster mitigation in high-relief mountainous regions.

1 Introduction

In eastern Tibet, the Jinsha, Mekong, and Salween - three of the largest Asian rivers - flow in parallel to each other and incise steep gorges, with up to 6 km of ridge-valley relief, while draining off the tectonically active margin of the Tibetan plateau (Larsen and Montgomery, 2012; Liu-Zeng et al., 2008). The topographically varied terrain carved by fluvial incision, in association with the monsoonal climate, fosters a biodiversity hotspot with one of the highest speciation rates in the world (Myers et al., 2000). Ongoing rapid incision in the upper reaches (e.g., Zhang et al., 2021) destabilizes hillslopes, leading to landslides, occasional river damming and associated landslide-lake outburst floods (LLFs) (e.g., Fan et al., 2020; Korup and Tweed, 2007). The extreme discharge of LLFs often entrain large volumes of sediments and are major drivers for geomorphic change. Yet, there is a lack of observations of the LLFs' catastrophic impacts on hillslopes (Baker, 2001; Turzewski et al., 2019), hindering the understanding of the geomorphic processes of LLFs and the development of hazards and landscape evolution models.

The extremely large water flux of LLFs to the receiving rivers is the most obvious phenomenon and has significant social impacts. For example, in A.D. 2000, a large rock avalanche dammed the Yigong River with an estimated maximum

impoundment of >2 km^3. The resulting flood led to record river level rise at gauging stations ~500 km from the landslide and caused major damage to infrastructures (such as roads and bridges) and losses of lives in India (Delaney and Evans, 2015). Recently, the Tangjiashan landslide dammed lake after the 2008 Wenchuan earthquake posed serious threats to the Mianyang city inhabited by millions of people (Fan et al., 2012a). A more astonishing LLF in 1920 BCE is supposed to flood the downstream Yellow River and even changed the ancient Chinese history (Wu et al., 2016).

Besides flooding havocs, LLFs have long been recognized as important geomorphic drivers on fluvial systems. Most works on geomorphic impacts of LLFs have been focused on their efficiency in sediment transportation and channel erosion (Cook et al., 2018; Turzewski et al., 2019). Bank undercutting and parallel retreat are the most-frequently reported consequences of LLF's lateral erosion (Korup and Tweed, 2007). Landslides related to bank undercutting along flood routes are regarded as instantaneous impacts of LLFs, which are often recognized by retrospective field reconnaissance or post-event image interpretations (Cook et al., 2018; Higaki and Sato, 2012). Intersecting with the LLF routes, these already-occurred landslides are easy to recognize (Cook et al., 2018). In addition to these instantaneous landslides, LLFs may also disturb upper hillslopes that adjacent to the river channel over longer periods, which are more difficult to recognize and often overlooked. Thus, there is a lack of observations on LLFs' impacts on these ongoing slope slippages.

Two landslides occurred on October 10, 2018, and November 10, 2018, near Baige along the Jinsha River. These successive landslides caused two mega floods (the peak discharges of the floods are ~10,000 and ~31,000 m^3/s, respectively) (Cai et al., 2020) on 12nd October and 12nd November 2018. In this study, the ongoing impacts of LLF on hillslope instability are investigated through quantitative measurements of downstream slope movements related to two upstream LLFs along the upper Jinsha River.

2 Materials and Methods

2.1 Two floods related to the Baige landslides in 2018

A slope near Baige village, Tibet Autonomous Region, China, failed twice in 2018 (Ouyang et al., 2019). The first landslide occurred on October 10, 2018, fully blocking the Jinsha River, forming a dammed lake with a maximum storage water of 0.29 km^3 (Fan et al., 2019). The lake started to drain naturally on October 12, 2018, leading to a first onsite flood wave with a peak discharge of 10,000m^3/s (Zhong et al., 2020). The first flood discharge finished on October 16, 2018 and there are no reports of economic damage during the first flood (Fan et al., 2019).

On November 3, 2018, the same slope collapsed again, leading to a second landslide dam, which fully blocked the Jinsha River. After November 8, 2018, several excavators were deployed to construct spillways. The lake started to drain through the spillway on November 12. The maximum water volume of the second lake was >0.52 km^3 (Fan et al., 2019). The second landslide lake caused a mega flood with a peak onsite discharge of 31,000 m^3/s near Baige (Zhong et al., 2020). This flood caused significant damages to major roads, schools, buildings and farms in the Diqing and Lijiang Prefectures, Yunnan

Province, ~ 500 km downstream of the Baige landslides. Fortunately, no casualties were reported during these two LLFs due to effective and timely evacuations.

Hillslopes on both sides along the Jinsha River were investigated for the downstream 100 km-long stretch from the Baige landslide (Fig. 1). The elevation of the region ranges from 2,500 m to 5,400 m, with a mean value of 4,100 m above sea level (*als.*). In the study reach, the Jinsha River cut through the Plateau and flows from north to south; the valley floor descends from 2,900 m *asl.* to 2,600 m *asl*. (Fig. 1) over ~ 80 km distance.

2.2 Slope displacements derived from the Sentinel-2 images

We used the coregistration of optically sensed images and correlation (COSI-Corr) method to derive subpixel horizontal slope deformation in Sentinel-2 image pairs (Leprince et al., 2007). The COSI-Corr method is a pixel matching method. To detect surface deformation, the method uses two images at a time, an earlier reference image and a later target image. Both images are transformed from the spatial domain to the frequency domain using the Fourier transformation (Leprince et al., 2007). Sub-pixel changes are detected by using phase changes in the frequency domain. Using the reference image from the earlier time, ground deformation can be derived from the target image in the later time. The principle of the method is to compare the difference in the reference image and the target image. There are two correlator engines to perform the procedure: The frequency and the statistical. The frequency correlator transforms the images into the Fourier domain and detect sub-pixel surface changes in the phase images, whereas the statistical correlator compares changes in the spatial domain (Leprince et al., 2007). The frequency correlator is more accurate to detect surface changes than the later correlator and is used in this work.

To perform the frequency correlator in the COSI-Corr, the initial and final window sizes are two major parameters to be defined. The final window is set no larger than the initial window size by default. For both windows, smaller sizes are sensitive to background noises, whereas larger window sizes often result in smooth results (Lacroix et al., 2018; Yang et al., 2020a). In this work, we used moderate window size combinations of 64 and 32 for the initial and final window sizes.

To detect slope deformation before and after the Baige floods, we used an image pair on November 13, 2015, and November 12, 2018, and a second image pair on November 12, 2018, and November 12, 2019. Images in these two pairs cover a large area from the Baige landslide to a 100 km downstream region along both banks of the Jinsha River (Fig. 1). Both image pairs are from the same date of different years to minimize uncertainties by having similar solar zenith/azimuth angles (Yang, 2020, Yang et al., 2020a).

We further analysed the Mindu section, ~80 km from the Baige landslide, where more moving hillslopes were detected. In this section, we composed 16 image pairs to detect the time series of slope displacements after the Baige floods. The dates of the reference and target images in these 16 image pairs are shown in Table 1. In this work, four reference images in January (3rd, 13rd, 16th) and February (12nd) 2017 are used. Acquisition dates of these reference images are very close to ensure no displacements occur among them, because slopes in this section are stable before October 2018 and have been moving since then (Fig. 3). We used the same stable zone near Mindu to correct the image shifts between the reference and the target images

3

with Yang et al. (2020b). In addition, we used two Sentinel-2 images in the summer months of July 15, 2017, and August 16, 2019, to map the width of the active channel before and after the 2018 floods.

Uncertainties in the derived surface deformation have several sources, such as DEM errors during orthorectification, solar angle differences between the reference and the target image, et al and can be estimated as the mean and standard deviation of displacements in a manually elected stable area (Bontemps et al., 2018; Lacroix et al., 2018; Yang et al., 2020a). In this work, we used the stable area as Yang et al. (2020b) near the MD-2 landslide.

Uncertainties in this method are often estimated by selecting a stable zone (Yang et al., 2020b). Although previous works demonstrated the capability of using similar method to detect surface deformation of up to 1/20 pixel size (Leprince et al., 2007; Stumpf et al., 2017), the smallest reliable displacements is 1/5 of the image pixel size (Yang, 2020).

Similar to the method used by Cook et al. (2018), we measured active river channel by manually interpreting active river channels from false colour composite Sentinel-2 images. Fresh bare land near river banks are major features to interpret active river channel. Topographic information from Google Earth are also used as an ancillary data during interpretation. The uncertainty of manually interpret active channel is one pixel size of the used optical imagery (10 m in this work).

3 Results

3.1 Magnitudes of the 2018 Baige LLFs

The nearest downstream hydrological station is the Batang station, which is 190 km away from the Baige landslide. The multi-year average discharge measured at the station is 924 m^3/s (Xiong et al., 2020). The recorded peak discharges at this station for the first and the second Baige floods are 7,850 m^3/s and 21,200 m^3/s, respectively. We collected 40-year records of annual peak discharges for the Batang station from 1953 to 2017 representing background climatic discharges (Fig. 2). Peak discharges caused by the Baige floods are 1.3 and 3.6 times larger than the recorded maximum annual peak discharge in 1954 (Duan et al., 2016). In addition, measured suspended sediment discharge for the first and second Baige floods are 2.3 and 4.5 times larger than the maximum annual peak sediment discharge (9.33 kg/m^3 in 1972), respectively.

Although the peak discharge of LLFs would decrease as it propagates downstream (Cook et al., 2018; Schwanghart et al., 2016; Cenderelli et al., 2001), the discharges recorded 190 km downstream the Baige landslide are still much higher than background climate values. This means that peak discharges would be much larger than normal climate discharges in the river section between the Baige landslide and the Batang station during these two floods. These exceptionally high discharges with record-high sediments would be much more efficient to erode river channels.

3.2 Post-flood slope movements along the Jinsha River

We identified at least nine post-flood moving slopes (Fig. 3) in the studied reach. Before the Baige floods in 2018 (2015.11-2018.11), very few slopes along the Jinsha River had displacements larger than 2 m, whereas there were widespread slope

movement with displacements larger than 2 m near the riverbank after the floods (2018.11-2019.11). All these newly emerged slope movements had larger deformations near the valley bottom and decreased progressively higher up along the hillslopes. Near the Mindu village, ~80 km from the Baige landslide, at least four hillslopes are slipping (d2 in Fig. 3). We showed displacements of these slopes in ten target images from January 13, 2018 to February 7, 2020 (Fig. 4) relative to the base images in early 2017 (Table 1). No displacements (> 2 m) were detected in the MD-1 (MD is short for the village Mindu), MD-2 and MD-4 hillslopes before the floods until late October and November 2018 (Fig. 4a-b). The toes of these hillslopes began to deform after the floods (since November 29, 2018, Fig. 4c-g). The deformation started from riverbanks and became larger with time and propagated upslope until the end of the study period (February 2020, Fig. 4g-j). At the MD-3 area, the hillslope deformation was less than 4 m from January 2017 to January 2018 (Fig. 4a), and less than 8 m by November 9, 2018 (Fig. 4c); however, an acceleration could be observed from November 2018 to January 2019 (Fig. 4d-e). There are some background noises on hillslopes and tributary catchments in Fig. 4, which is irrelevant to the 2018 floods.

We further selected three representative points, each on the MD-1, MD-2 and MD-3 landslides, respectively, and measured their cumulative movements and velocity at 16 different dates (Table 1) from January 2018 to February 2020 (Fig. 5). The points on MD-1 and MD-2 landslides show similar temporal patterns. Movement for both points before November 2018 is minimal (< 0.18 cm/d from February 2017) compared to 4.55 cm/d from November 2018 to April 2019. Despite the Nov. 12, 2018 image was acquired during the second flood on Nov. 12, undetected displacements from 2015 to Nov. 12 2018 suggests that the first flood has little post-effect on slow deformations and cannot be detected in a short time. Cumulative displacements at the MD-1 and MD-2 points continued to increase from ~8 m to ~ 12 m since then. Significant acceleration of the slope movement was also found for the point on MD-3 landslide. The MD-3 point moved 1.52 cm/d (uncertainty <0.26 cm/d) before November 9, 2018, and then increased to 4.84 cm/d (uncertainty <0.96 cm/d) from November 2018 to February 2019. No additional displacements were detected after February 2019, which is due to collapse of the slope at the point.

3.3 Concurrent landslides and channel expansion during the 2018 floods

Active channel width increased for almost all parts of the study area (Fig. 6). There was widespread lateral erosion of the Jinsha River bank in the form of riverbank undercutting and parallel retreat. The successive LLFs increased the mean width of the active channel from 96.33 m to 148.56 m. The river width expanded 52.2 m on average after the 2018 floods. Lateral erosion to the Jinsha riverbanks led to undercutting of slopes, which propagated up hillslope and could have been the direct trigger for the expansion of landslides existing before the Baige LLFs. In addition, we observed a few new landslides (Fig. 7), which could also be concurrent with the 2018 LLFs. We further measured the area of these concurrent landslides and postevent moving slopes with deformation >2 m in January 2020. The areas of these concurrent landslides and moving slopes were 2.18×10^5 m^2 and 11.86×10^5 m^2, respectively. The areal extent of the moving slopes (with deformation > 2 m) was 5.4 times that of the concurrent landslides. Although most of these moving slopes and the concurrent landslides occurred in the reach that experienced significant increase in river channel width, there seems to be no relations between the increase (rate) of the channel and the maximum measured displacements of the moving slopes (Appendix 3).

The influence of the 2018 floods on adjacent hillslopes could be larger than reported here. In this work, the method we use can reliably track slope deformation >2 m (Stumpf et al., 2017; Yang, 2020) and we only monitored the downstream riverbanks for less than 2 years. It is possible that there could be more slow-moving slopes with cumulative displacements <2 m but not detected by our method.

4 Discussion

4.1 Implications for mountain hazards

Outbursts of landslide lakes present severe flooding threats to downstream communities (Delaney and Evans, 2015; Ling and Evans, 2014; Dai et al., 2005; Fan et al., 2012a). Landslide dams can be formed at more diverse locations along the river (Liu et al., 2019) than other types of natural dams, such as glacier or moraine dams, which are usually located in highlands near riverheads and are far from human communities (Cook et al., 2018). Therefore, LLFs pose more serious threats to humans due to their closer distances to densely populated regions.

The observations in this study show that the 2018 Baige landslides destabilized some major downstream hillslopes tens of kilometres away. If these hillslopes fail subsequently, they may cause further disruptions to the main channel, forming a domino effect of "landslide-LLF-landslide" hazard chains. For example, Yang et al. (2020b) found the size of the moving MD-2 slope is larger than the Baige landslide, whereas the river directly below MD-2 is narrower than the later one, indicating high risk of blocking the channel once the landslide occur. If the MD-2 slope failed, the risk of blocking the river would be higher. This possible process demonstrates the propagation of LLF hazards downstream, which has not been given enough attention in the past, but should be considered in future disaster mitigation measures. The findings of this work also have important implications for the ongoing construction of the Sichuan-Tibet railway, which runs through deepest gorges along the Jinsha, Mekong, and Salween Rivers.

4.2 Possible mechanism for hillslope slippage

To form the "landslide-LLF-landslide" hazard chain, weak riverbank hillslopes may be an important prerequisite. In our study area, we found all slopes with tensile cracks had deformations after the Baige floods (Fig. 8). These tensile cracks may be joint results of interactions among active regional tectonics, weak rock types, large slope gradients and intense precipitations: 1) The Jinshajiang fault zone is the main fault zone in this study area. GPS measurements show that the near-east-west shortening rate of the fault zone is 2~3mm/a (Chen et al., 1998; 2000). However, there is no strong earthquakes occurred in the past 100 years for this section of the fault zone. Despite this, faults with prolonged activity of fault motion produce damage zones and crushing rocks along the Jinsha suture, leading to high landslide susceptibility for this study area (Cao et al., 2016). 2) The strata of the study area mainly include Mesoproterozoic metamorphic rock of gneiss, quartz schist and metagranulite, which can be easily weathered to form layers with weak shear strength during rainfall. 3) The landscape of the study area is deeply incised by with high slope gradients greater than the angle of repose (20-30degree, Larsen and Montgomery, 2012). 4) >60%

6

of the precipitation occurs from July to September. The Monsoon-driven precipitation, characterized by intense storms with large-magnitude and short-duration rainfall is another stimulus for landsliding.

190 Besides deformations on slopes with tensile cracks, we also found some deformations on slopes that have no visible tensile cracks. However, both types of slopes had bank collapses adjoining the active river channel, though the former slope type has much larger area of deformations. The removal of buttressing by the 2018 LLFs' erosion may attribute to the hillslope slippage in downstream reaches, which is substantiated by our observation that detected deformations are larger near the riverbank and decrease in concentric ellipses upslope.

195 Figure 3 indicate the velocity of three slope deformations. All these slopes showed increased moving speed immediately after the floods, indicating that the Baige floods probably accelerated slope slippage. For MD-1, the speed decreased quickly after the floods, which may indicate the deteriorations of the floods' effect with time. For MD-2, we can also see similar deformation-time pattern before May 2019. The deformation continued with a lower speed from May 2019 to January 2020. The deformation of slopes may be related to precipitation or river discharge. As we do not have daily or monthly hydrological

200 data, we analysed the GPM monthly precipitation from Nov. 2018 to Feb. 2020 (Appendix A2). Rainy season in 2019 begins from March to October. The beginning of the rainy season in March may explain the acceleration of MD-1 and 2 in March. The deformation continued during rainy season (March to October). However, the acceleration of MD-2 after 18 Jan. 2020 does not agree with precipitation change and should be explained by other triggers.

4.3 Implications for geomorphic processes

205 Previous works about the influence of LLFs on hillslope instability along major rivers are hypothetical and lack direct observations (Cook et al., 2018; Higaki and Sato, 2012). Widespread active channel expansions and bank collapses after the Baige floods confirms that mega-floods are major drivers of landscape evolution (Baynes et al., 2015; Lamb et al., 2014). Our finding that the Baige floods accelerated slope slippages support the claim that landsliding is a key process to link fluvial incision and tectonics in landscape evolution (Larsen and Montgomery, 2012). Mega-floods can cause both instant landslides

210 in terms of bank collapses (Cook et al., 2018) and post-flood landslides by destabilizing hillslopes along fluvial channels that fail in later years. However, much focus has been placed on the immediate hazards of LLF such as the instantaneous downstream floods and inundations (Dai et al., 2005; Delaney et al., 2015; Fan et al., 2012a). The lack of observations on post-flood landslides hinders our understanding on the long-term impacts of mega floods to landslides, landscape evolution and related risks. This work shows that in addition to immediate (or concurrent) landslides (Cook et al., 2018; Higaki and Sato,

215 2012), the impact of LLF lateral erosion could propagate uphill by disturbing adjacent hillslope stability for a prolonged period, illustrating the dynamic response of mountain hillslopes to channel incision.

Infrequent catastrophic floods could play an important role in landscape evolution (Cook et al., 2018). Our finding that the mean active channel width increased by 54.2% after the 2018 LLFs indicate that rare catastrophic events could leave a disproportionate footprint on local landscapes. Compared to monsoonal discharges, LLFs can cause extensive bank erosions

220 and efficiently expand active river channels by undercutting hillslope bases and bank retreat. This is consistent with previous

7

findings bedrock canyons on the surfaces of Mars and Earth are probably caused by infrequent catastrophic floods instead of uniform, steady erosion from background runoff (Baynes et al., 2015; Keisling et al., 2020; Lamb et al., 2014; Lamb and Fonstad, 2010; Larsen and Lamb, 2016; Malatesta et al., 2017).

However, quantitative assessment of the role of LLFs on the long-term landscape evolution awaits for future research. First, the relationship between the magnitude and frequency of LLFs should be constrained. The volume of impoundment water and downstream channel morphology, which is site specific, determines the severity/magnitude of an LLF (Fan et al., 2012b). Landslide triggers, such as large-magnitude earthquakes and high-intensity storms, control the frequency of LLFs. Strong earthquakes can trigger numerous landslides within river systems and form many landslide-dammed lakes (Fan et al., 2012b), the outbursts of which could accelerate the flush of postseismic landslide debris (Croissant et al., 2017). In addition, the strength of hillslopes along the LLF pathway should also be constrained. Hillslopes composed of weaker bedrock or repeatedly damaged by seismicity could have more slope erosions after the occurrence of LLFs. Despite these related but poorly understood questions, our observations indicate that LLFs could significantly improve the efficiency of regional erosion and can be an important internal variable that modulates regional erosion.

5 Conclusions

In October and November 2018, two large landslides occurred on the same slope near the Baige village along the Jinsha River, leading to two successive LLFs downstream. Besides three new landslides and widespread lateral erosion, we found the LLFs destabilized at least nine hillslopes, which progressively deformed over the following year within a hundred kilometres downstream of the landslide. Bank undercutting and parallel retreat are prevalent after the Baige floods, which probably activated these slopes by removing their buttresses. Landslide hazards propagate to long-range downstream regions by releasing mega floods to undercut hillslopes along river channels, leading to more destabilized hillslopes. Persistent monitoring of slope deformation along major rivers may be a viable way to detect possible hazards in remote mountain regions.

Compared to LLF-triggered concurrent landslides, subsequent slowly moving slopes are less easily recognized and thus often overlooked. Realizing that LLFs may lead to more hillslope slumping, in larger areal extent, and during the prolonged period afterwards could help researchers to obtain a holistic picture of LLFs' impacts and improve geomorphic models of landscape evolution. In the future, LLF contributions to hillslope erosion may be constrained by quantifying the magnitude-frequency relationship.

Appendix A1

We searched all earthquakes with magnitude >4.5 and <500km from the Mindu-1, MD-2 and MD-3 landslides in the last hundred years. There are 1026 earthquakes occurred with the largest magnitude of Mw8.6. The magnitudes of 54 earthquakes are ≥6.0.

The finding that all slopes with tensile cracks have deformations after the floods indicates to form the "landslide-LLF-landslide" hazard chain, weak riverbank hillslope may be an important prerequisite. Tectonic activities such as earthquakes can usually weaken the strength of hillslopes.

Appendix A2

As we examined from very high spatial images on Google Earth, all these three slopes have tensile cracks. Compared with the MD-3 slope, MD-1 and MD-2 are all stable slopes before the floods. Their consistent behaviours before and after the floods indicate that both LLFs indeed accelerate slope slippage. We agree with the reviewer that the deformation of slopes may be related to precipitation or river discharge, but we do not have daily or monthly hydrological data. We collected GPM monthly precipitation from Nov. 2018 to Feb. 2020 (Fig. A2). Rainy season in 2019 begins from March to October. The beginning of the rainy season in March may explain the acceleration of MD-1 and 2 in March. The deformation continued during rainy season (March to October). However, the acceleration of MD-2 after 18 Jan. 2020 should be explained by other triggers except precipitation.

Appendix A3

We made a plot between the increase (rate) of the channel and the maximum measured displacements, as shown in Figure below. It shows no relation between the two variables. This is because slope stability is determined by the integrity of bedrocks in the first order (Gallen et al., 2015).

Data availability

The Sentinel-2 remote sensing data can be accessed from the Sentinel-hub (https://www.sentinel-hub.com/). The ALOS World 3D-30m DEM are available on the JAXA website (https://www.eorc.jaxa.jp/ALOS/en/aw3d30/index.htm).

Author contributions

The manuscript was written by WY with major contribution by JF and JLZ. WY processed the data. WY, JF and JLZ interpreted the results. All authors reviewed and approved the manuscript.

Competing interests

The authors declare that they have no conflict of interest.

References

Baker, V. R.: Water and the Martian landscape. Nature, 412(6843), 228-236, 2001.

Baynes, E.R.C., Attal, M., Niedermann, S., Kirstein, L.A., Dugmore, A.J., Naylor, M. Extreme flood erosion dominates canyon evolution. PNAS, 112 (8), 2015.

Bontemps, N., Lacroix, P., Doin, M.P. Inversion of deformation fields time-series from optical images, and application to the long term kinematics of slow-moving landslides in Peru. Remote Sens. Environ., 210, 144-158, 2018.

Cai, Y., Cheng, H., Wu, S., Yang, Q., Wang, L., Luan Y., and Chen, Z.: Breaches of the Baige Barrier Lake: Emergency response and dam breach flood. Sci. China Technol. Sci., 63(7), 1164-1176, 2020.

Cao, C., Wang, Q., Chen, J., Ruan, Y., Zheng, L., Song, S., Niu, C. Landslide Susceptibility Mapping in Vertical Distribution Law of Precipitation Area: Case of the Xulong Hydropower Station Reservoir, Southwestern China. Water, 8(7),270, 2016.

Cenderelli, D. A. and Wohl, E. E.: Peak discharge estimates of glacial-lake outburst floods and "normal" climatic floods in the Mount Everest region, Nepal. Geomorphology, 40(1-2), 57-90, 2001.

Chen, Z., Burchfiel, B. C., Liu, Y., King, R. W., Royden, L. H., Tang, W., Wang, E., Zhao, J., Zhang, X. Global Positioning System measurements from eastern Tibet and their implications for India/Eurasia intercontinental deformation. J. Geophys. Res. Solid Earth, 105(B7), 16215-16227, 2000.

Chen, Z., Zhang, X., Shen, F., Zhao, J., Liu, Y., Tang, W., Bruchfiel, B.C., King, R.W., Royden, L.H. GPS Monitoring of Crustal Movement in Southwest China. Chin. Sci. Bull., 44(8), 851-854, 1998.

Cook, K. L., Andermann, C., Gimbert, F., Adhikari, B. R., and Hovius, N.: Glacial lake outburst floods as drivers of fluvial erosion in the Himalaya. Science, 362(6410), 53, 2018.

Croissant, T., Lague, D., Steer, P., and Davy, P.: Rapid post-seismic landslide evacuation boosted by dynamic river width. Nat. Geosci., 10, 680–684, 2017.

Dai, F. C., Lee, C. F., Deng, J. H., and Tham, L. G.: The 1786 earthquake-triggered landslide dam and subsequent dam-break flood on the Dadu River, southwestern China. Geomorphology, 65(3), 205-221, 2005.

Delaney, K. B. and Evans, S. G.: The 2000 Yigong landslide (Tibetan Plateau), rockslide-dammed lake and outburst flood: Review, remote sensing analysis, and process modelling. Geomorphology, 246, 377-393, 2015.

Duan, W., He, B., Nover, D., Fan, J., Yang, G., Chen, W., Meng, H., and Liu, C.: Floods and associated socioeconomic damages in China over the last century. Nat. Hazards, 82, 401-413, 2016.

Fan, X., Dufresne, A., Siva Subramanian, S., Strom, A., Hermanns, R., Tacconi Stefanelli, C., Hewitt, K., Yunus, A.P., Dunning, S., Capra, L., Geertsema, M., Miller, B., Casagli, N., Jansen, J.D., and Xu, Q.: The formation and impact of landslide dams – State of the art. Earth-Sci. Rev., 203, 103116, 2020.

Fan, X., Tang, C., van Westen, C., and Alkema, D.: Simulating dam-breach flood scenarios of the Tangjiashan landslide dam induced by the Wenchuan Earthquake. Nat. Hazard Earth Sys., 12(10), 3031-3044, 2012a.

Fan, X., van Westen, C. J., Xu, Q., Gorum, T., and Dai, F.: Analysis of landslide dams induced by the 2008 Wenchuan earthquake. J. Asian Earth Sci., 57, 25-37, 2012b.

Fan, X., Xu, Q., Alonso-Rodriguez, A., Subramanian, S. S., Li, W., Zheng, G., Dong, X., and Huang, R.: Successive landsliding and damming of the Jinsha River in eastern Tibet, China: prime investigation, early warning, and emergency response. Landslides, 16(5), 1003-1020, 2019.

Gallen, S.F., Clark, M.K., Godt, J.W. Coseismic landslides reveal near-surface rock strength in a high-relief, tectonically active setting. Geology, 43(1), 11-14, 2015.

Higaki, D. and Sato, G.: Erosion and sedimentation caused by glacial lake outburst floods in the Nepal and Bhutan Himalayas. Global Environ. Res., 16(1), 71-76, 2012.

Keisling, B. A., Nielsen, L. T., Hvidberg, C. S., Nuterman, R., and DeConto, R. M.: Pliocene–Pleistocene megafloods as a mechanism for Greenlandic megacanyon formation. Geology, 48(7), 737-741, 2020.

Korup, O. and Tweed, F. Ice, moraine, and landslide dams in mountainous terrain. Quaternary Sci. Rev., 26(25-28), 3406-3422, 2007.

Lacroix, P., Bièvre, G., Pathier, E., Kniess, U., Jongmans, D. Use of Sentinel-2 images for the detection of precursory motions before landslide failures. Remote Sens. Environ., 215, 507-516, 2018.

Larsen, I.J. and Lamb, M.P. Progressive incision of the Channeled Scablands by outburst floods. Nature 538:229-232, 2016.

Larsen, I. J. and Montgomery, D. R.: Landslide erosion coupled to tectonics and river incision. Nat. Geosci., 5(7), 468-473, 2012.

Lamb, M. and Fonstad, M. Rapid formation of a modern bedrock canyon by a single flood event. Nature Geosci., 3, 477–481, 2010.

Lamb, M.P., Mackey, B.H., Farley, K.A. Amphitheater-headed canyons formed by megaflooding. PNAS, 111 (1), 57-62, 2014.

Leprince, S., Barbot, S., Ayoub, F., and Avouac, J.: Automatic and precise orthorectification, coregistration, and subpixel correlation of satellite images, application to ground deformation measurements. IEEE T. Geosci. Remote, 45 (6), 1529-1558, 2007.

Ling, S. and Evans S. G.: GIS-based analysis of 1933 Diexi Landslides and dam breach on the Min River, Sichuan, China, paper presented at EGU General Assembly Conference Abstracts, 2014.

Liu, W., Carling, P. A., Hu, K., Wang, H., Zhou, Z., Zhou, L, Liu, D., Lai, Z., and Zhang, X.: Outburst floods in China: A review. Earth-Sci. Rev., 197, 102895, 2019.

Liu-Zeng, J., Tapponnier, P., Gaudemer, Y., and Ding, L.: Quantifying landscape differences across the Tibetan plateau: Implications for topographic relief evolution. J. Geophys. Res-Earth, 113(F4), F04018, 2008.

Malatesta, L. C., Prancevic, J. P., and Avouac, J. P.: Autogenic entrenchment patterns and terraces due to coupling with lateral erosion in incising alluvial channels. J. Geophys. Res-Earth, 122(1), 335-355, 2017.

Myers, N., Mittermeier, R. A., Mittermeier, C. G., da Fonseca, G. A. B., and Kent, J.: Biodiversity hotspots for conservation priorities. Nature, 403, 853-858, 2000.

Ouyang, C., An, H., Zhou, S., Wang, Z., Su, P., Wang, D., Chen, D., and She, J.: Insights from the failure and dynamic characteristics of two sequential landslides at Baige village along the Jinsha River, China. Landslides, 16, 1397-1414, 2019.

Schwanghart, W., Worni, R., Huggel, C., Stoffel, M., and Korup, O.: Uncertainty in the Himalayan energy–water nexus: estimating regional exposure to glacial lake outburst floods. Environ. Res. Lett., 11(7), 074005, 2016.

Stumpf, A., Malet, J. P., and Delacourt, C.: Correlation of satellite image time-series for the detection and monitoring of slow-moving landslides. Remote Sens. Environ., 189, 40-55, 2017.

Turzewski, M. D., Huntington, K. W., and LeVeque, R. J.: The Geomorphic Impact of Outburst Floods: Integrating Observations and Numerical Simulations of the 2000 Yigong Flood, Eastern Himalaya. J. Geophys. Res-Earth, 124(5), 1056-1079, 2019.

Wu, Q., Zhao, Z., Liu, L., Granger, D.E., Wang, H., Cohen, D.J., Wu, X., Ye, M., Bar-Yosef, O., Lu, B., Zhang, J., Zhang, P., Yuan, D., Qi, W., Cai, L., and Bai, S.: Outburst flood at 1920 BCE supports historicity of China's Great Flood and the Xia dynasty. Science, 353(6299), 579, 2016.

Xiong, M., Li, J., and Chen, Y.: Runoff Trend and Natural Driving Force in the Upper Jinsha River. J. Water Resour. Res., 9(3), 235- 248, 2020.

Yang, W.: Selecting the best image pairs to measure slope deformation. Sensors, 20(17), 4721, 2020.

Yang, W., Wang, Y., Wang, Y., Ma, C., and Ma, Y.: Retrospective deformation of the Baige landslide using optical remote sensing images. Landslides, 17(3), 659-668, 2020a.

Yang, W., Liu, L., and Shi, P.: Deriving slope movements for an imminent landslide along the Jinsha river. Nat. Hazard Earth Sys., 20, 3215-3224, 2020b.

Zhang, J., Yang, H., Liu-Zeng, J., Ge, Y., Wang, W., Yao, W., and Xu, S.: Reconstructing the incision of the Lancang River (Upper Mekong) in southeastern Tibet below its prominent knickzone using fluvial terraces and transient tributary profiles. Geomorphology, 376, 107551, 2021.

Zhong, Q., Chen, S., Wang, L., and Shan, Y.: Back analysis of breaching process of Baige landslide dam. J. Hydrol., 17, 1681-1692, 2020.

12
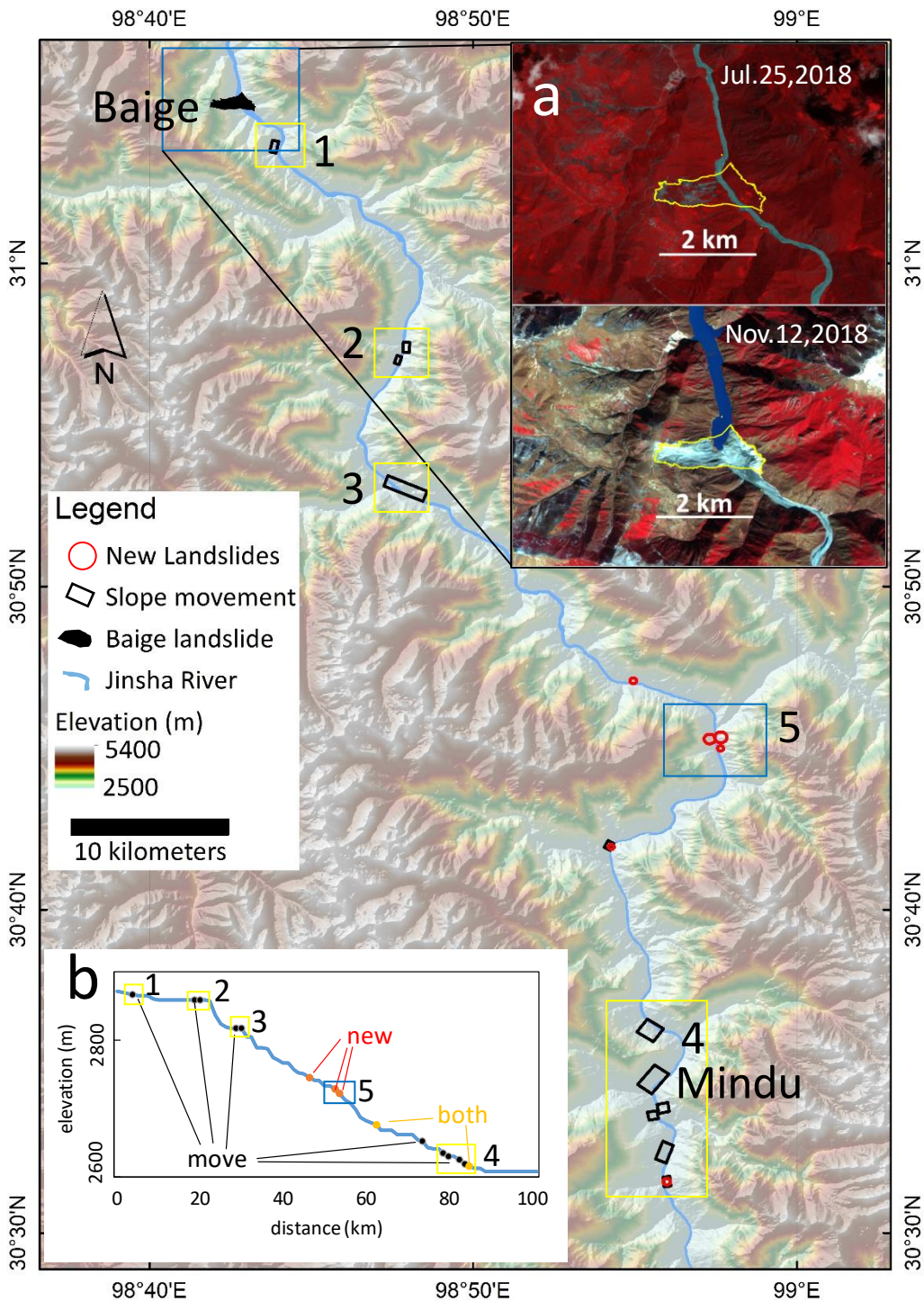
Figure 1: Map of the Jinsha River study region. Black rectangles are moving slopes detected after the Baige floods. Red circles are new landslides after the floods. Yellow rectangles with black numbers 1 to 4 are map extents shown in Figure 3a-d. Blue rectangles

375 with the black number 5 is the map extent for Figure 6. (A) Two Sentinel-2 images were taken before the Baige landslide in July 2018 (top) and after in November 2018 (bottom). (B) Longitudinal profile of the Jinsha River in this section from the ALOS World 3D-30m DEM, and the localities of new landslides and moving slopes are marked. The Jinsha River is digitized by the authors from Sentinel-2 images before the 2018 floods.
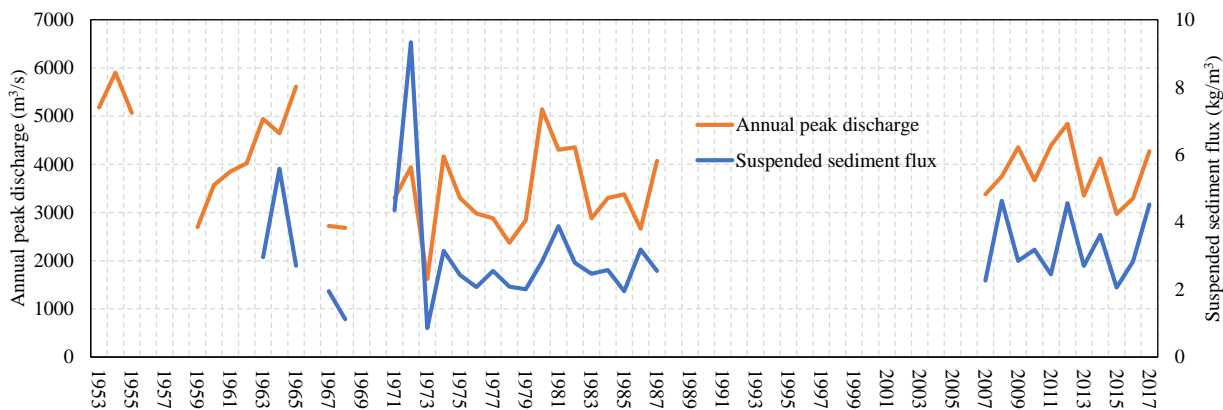
380 Figure 2. Multi-year peak discharge and suspended sediment flux at the Batang station. Note the discharges for the 2018 Baige floods are 7,850 m^3/s and 21,200 m^3/s, respectively. The suspended sediment fluxes are 21.6 kg/m^3 and 42 kg/m^3, respectively. Note multi-year gaps in the data available, partly due to the remoteness of the station. Despite the gaps, any event with discharge larger than those in 1954 would be recorded.

385
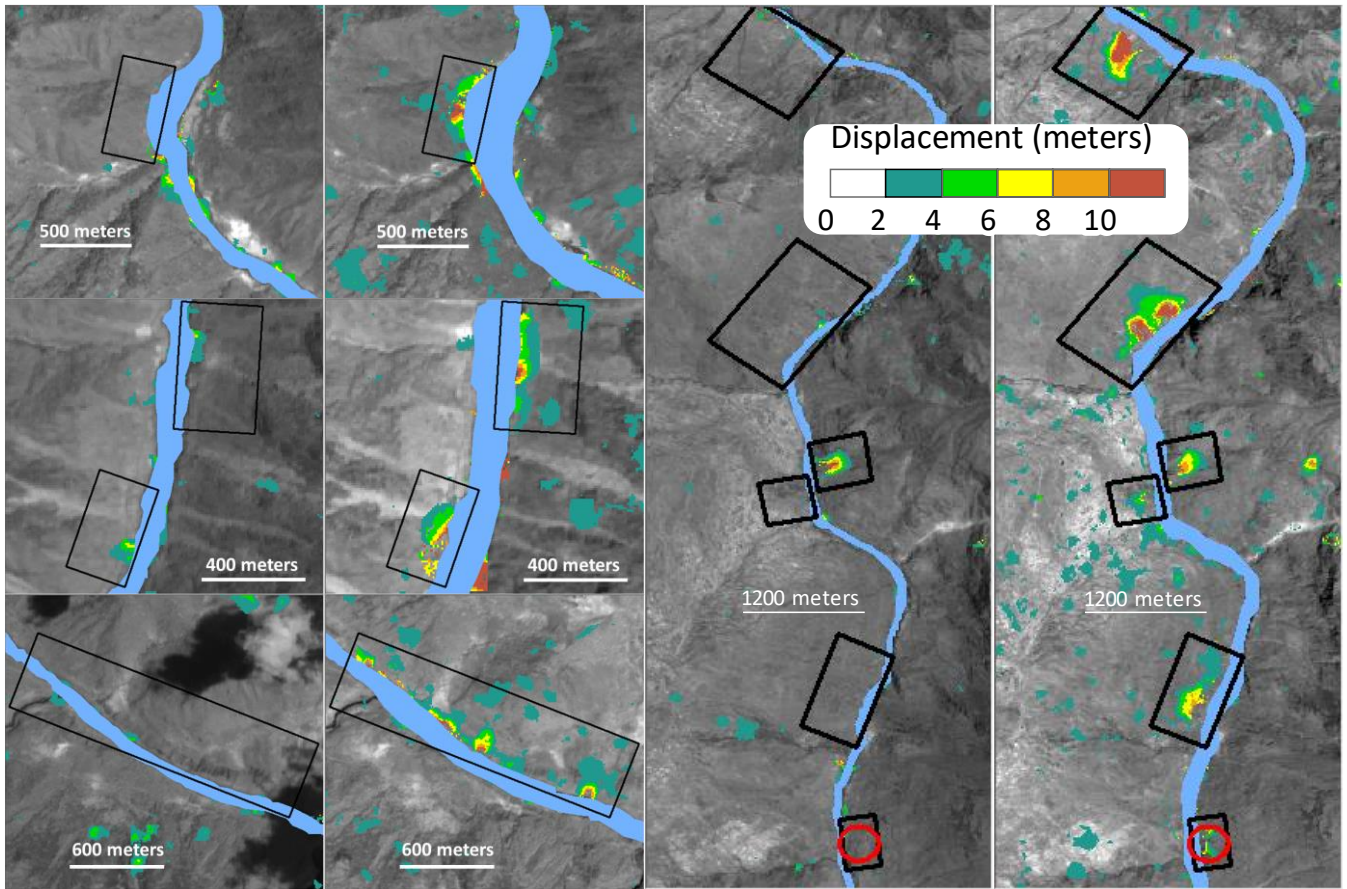
Figure 3. Moving slopes in four selected sections along the Jinsha River (a-d) before (2015.11-2018.11) and after (2018.11-2019.11) the Baige floods. Left subplots (a1, b1, c1, d1) are preflood results and right subplots (a2, b2, c2, d2) are postflood results. MD is short for the village Mindu. Background images are cloud-free grey scale Sentinel-2 images before and after the 2018 floods. Red
390　**circles indicate concurrent landslides and black squares are slope slippages.**
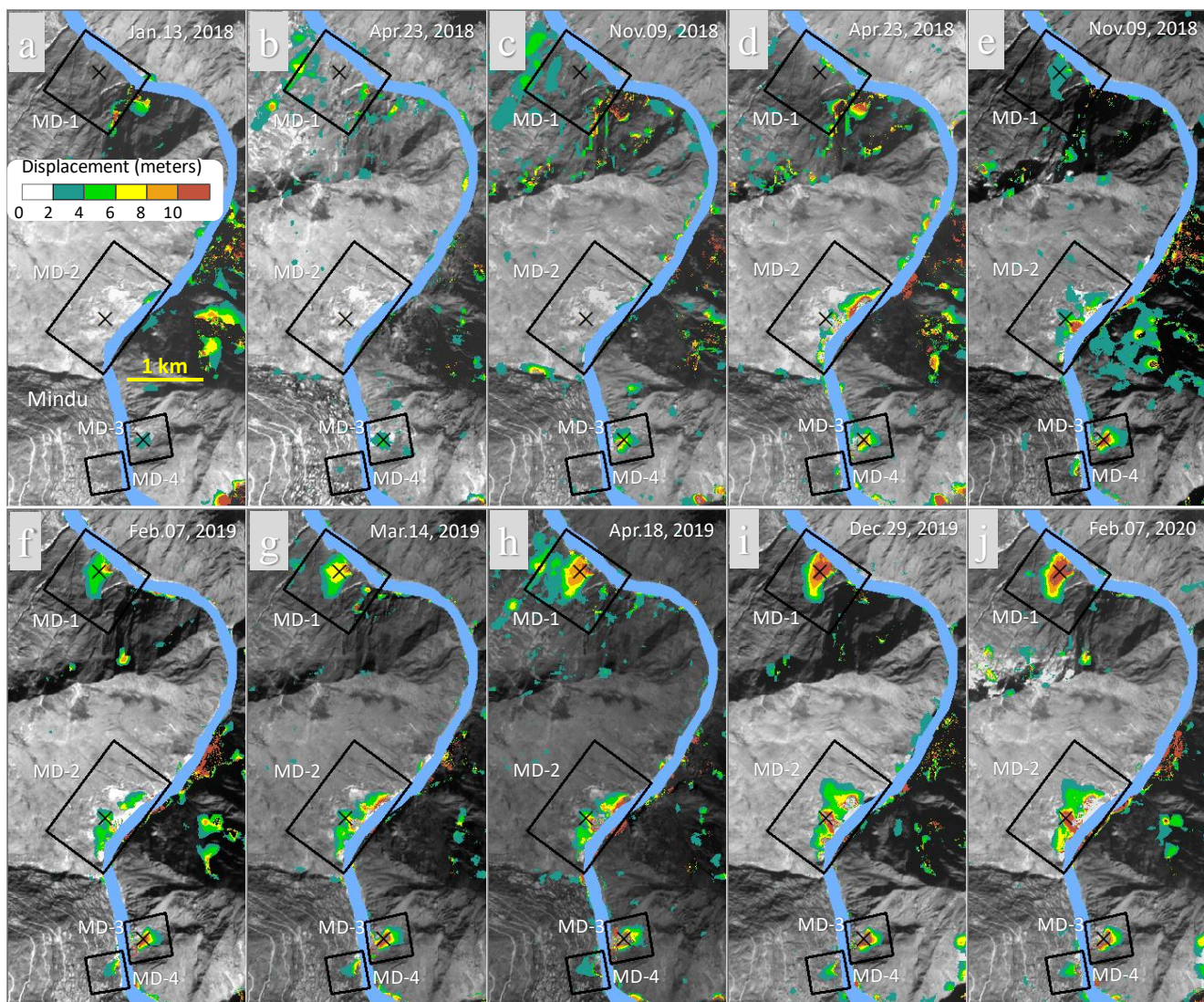
Figure 4. Cumulative hillslope displacements near the Mindu village at different times between early 2018 and early 2020, using the early 2017 image (either January or February) as the reference. Cumulative displacement (a-b) before the first Baige flood, (c) between the two floods, and (d-j) at different times between November 29, 2019 and February 07, 2020. Background images are also respective target Sentinel-2 images of the ending date for the calculation.
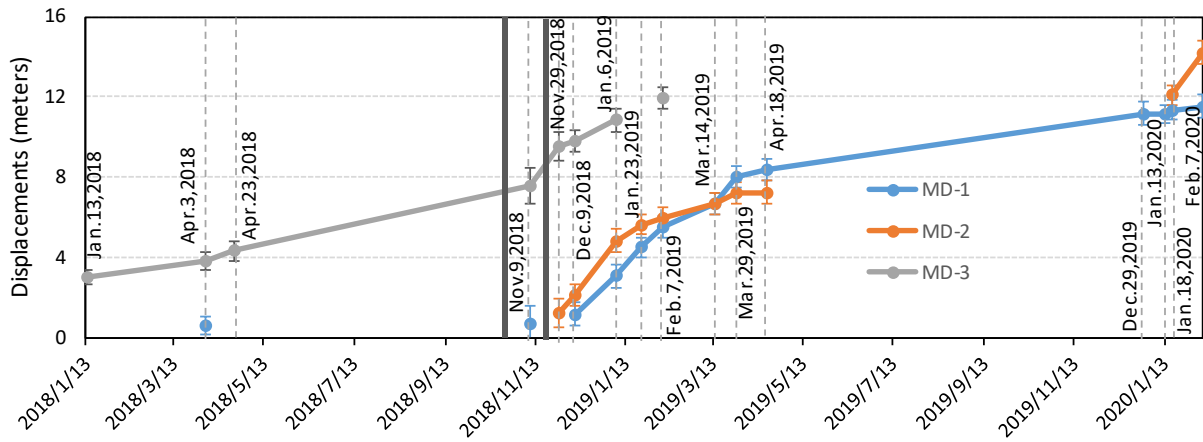
Figure 5. Cumulative displacements of three points (crosses in Figure 3) on three slopes near Mindu village (Two black vertical lines indicate the occurrence date of the Baige outburst floods in late October and November 2018). No displacement data for MD-2 during March 2019 and January 2020, due to low image quality.
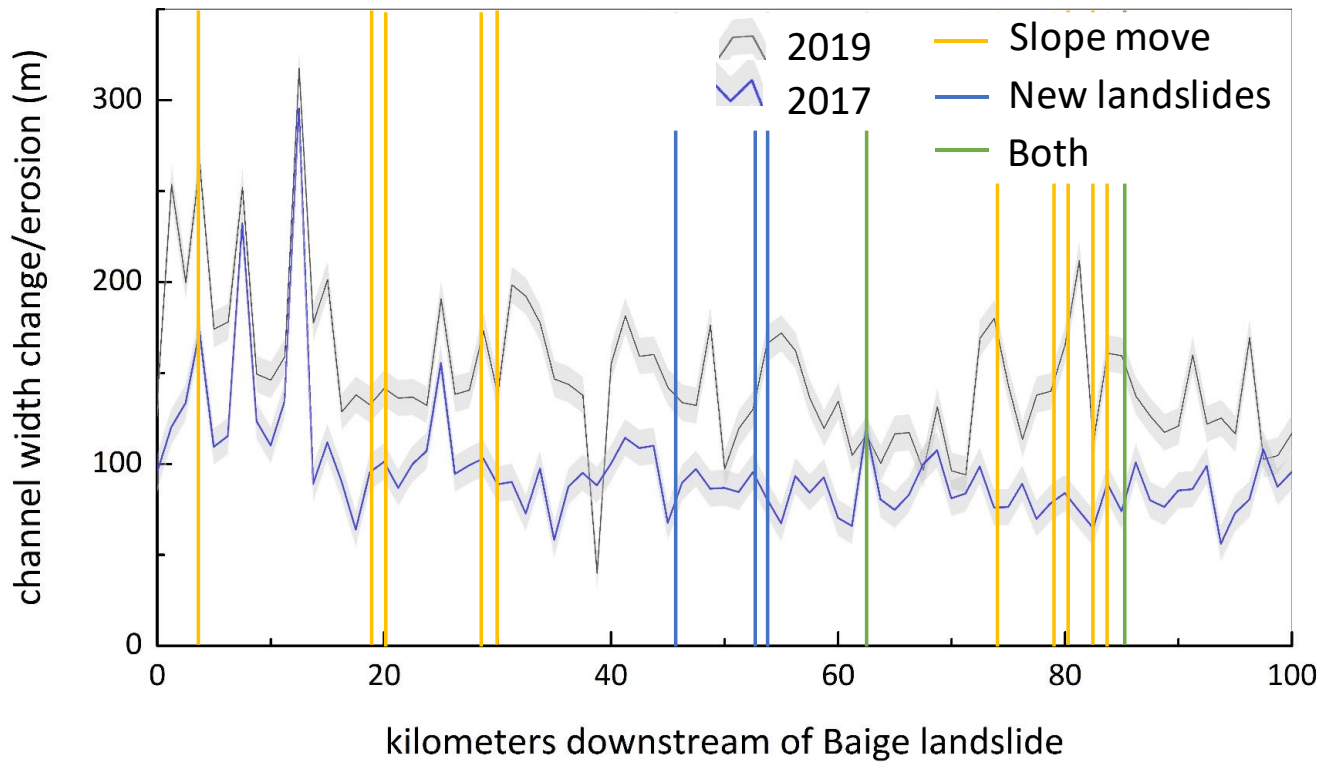
Figure 6. River widths before and after the Baige floods. The gray shadings indicates an uncertainty of ±1 pixel in the Sentinel-2 imagery.

405
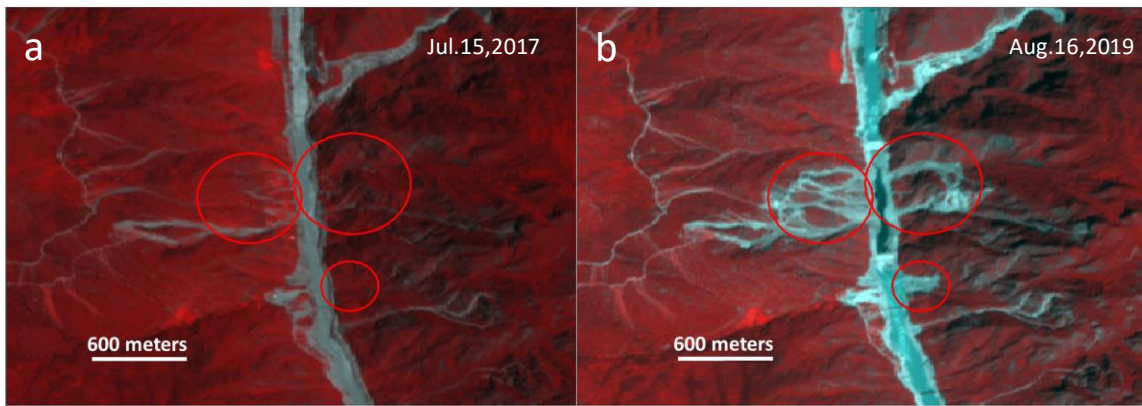
Figure 7. Concurrent landslides related to the Baige floods. False composite Sentinel-2 images are acquired on July 15, 2017 (a) and August 16, 2019 (b). The spatial extent of this area is shown as the rectangle 5 in Figure 1.

410

19

a

MD-1

500 m

b

MD-2

500 m
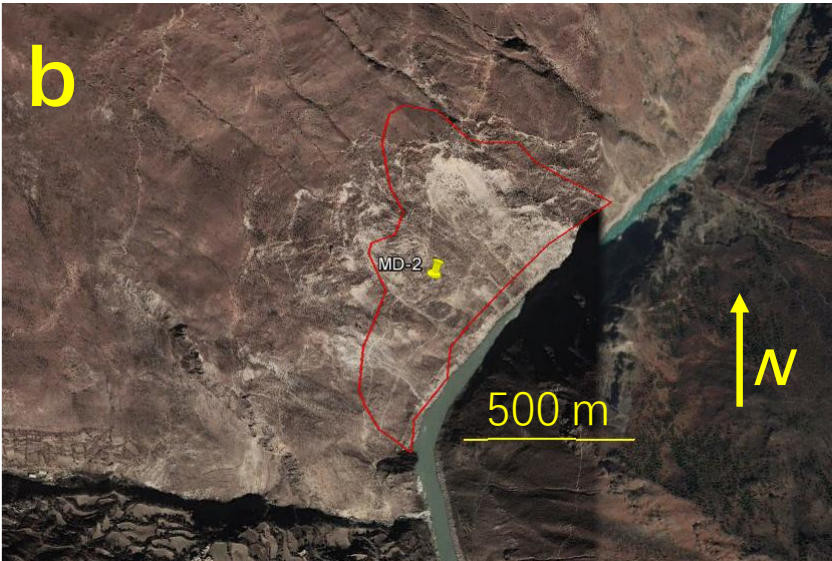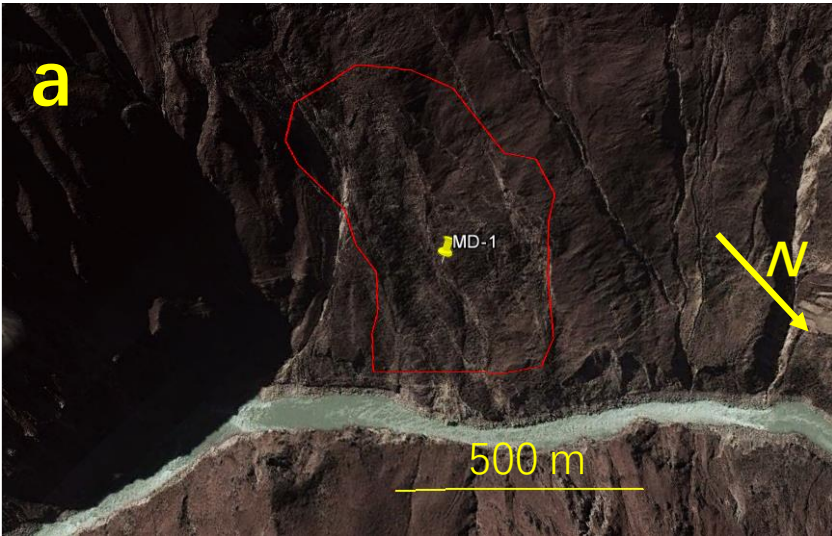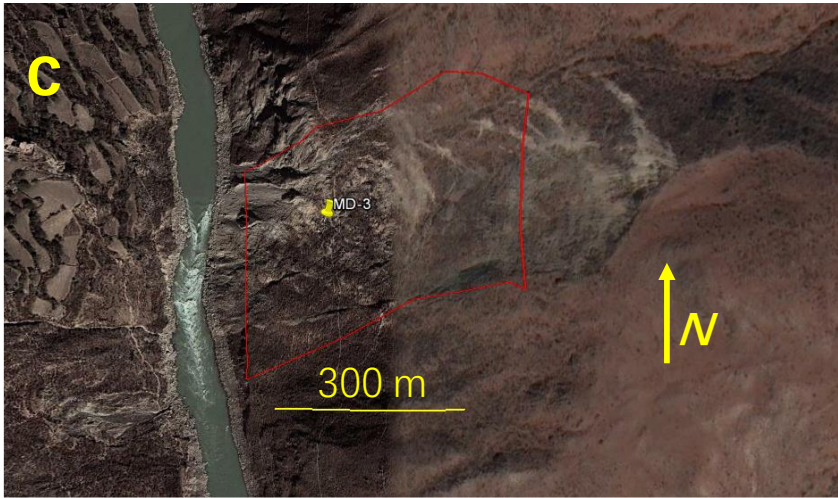
Figure 8. Tensile cracks of major hillslopes before the 2018 Baige floods as seen from high-spatial-resolution images from © Google Earth.
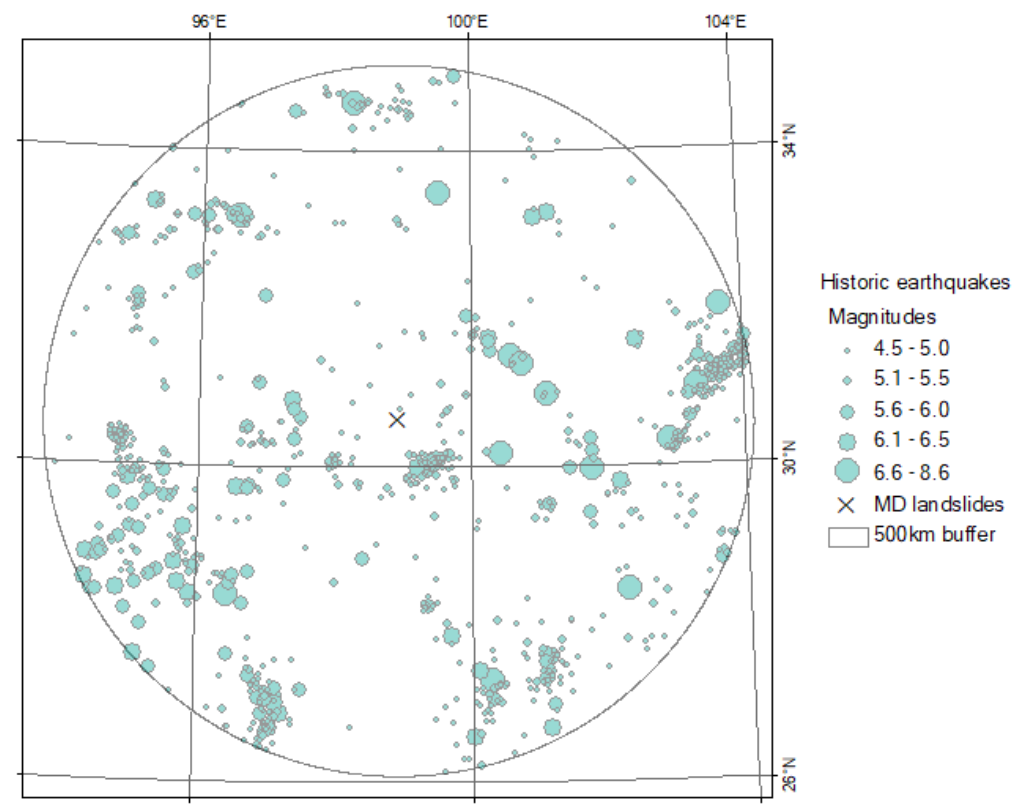
Figure A1. Historic earthquakes with magnitudes >4.5, within 500km from the MD-1, MD-2 and MD-3 landslides. Earthquake
420   events were searched and downloaded from the USGS website (https://earthquake.usgs.gov/earthquakes/search/).
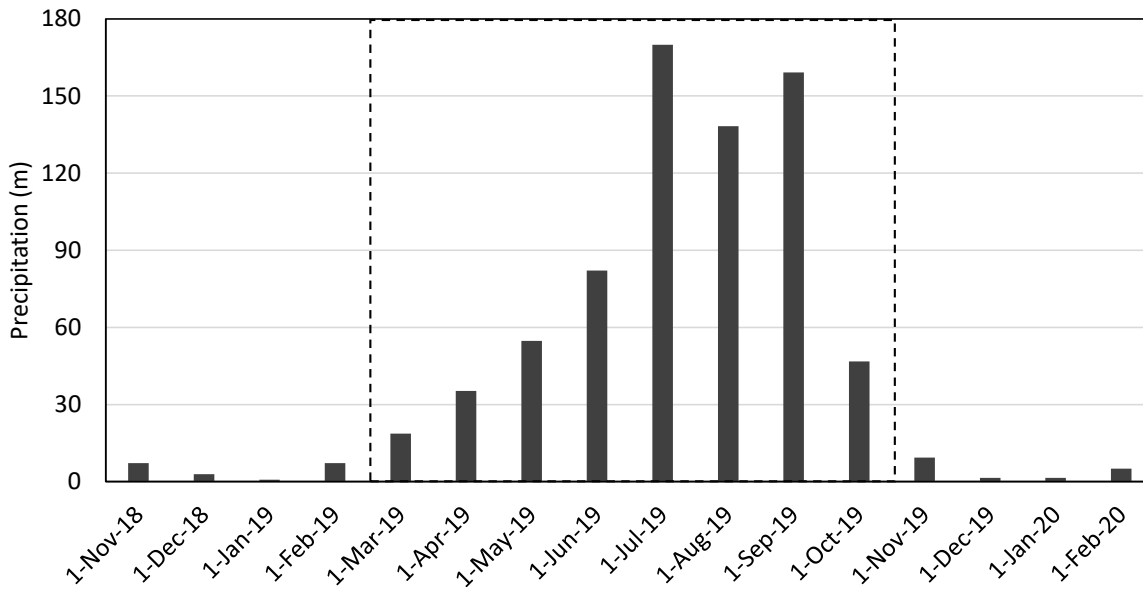
Figure A2. Monthly GPM precipitation near the MD-1, MD-2 and MD-3 slopes. The precipitation were downloaded from the
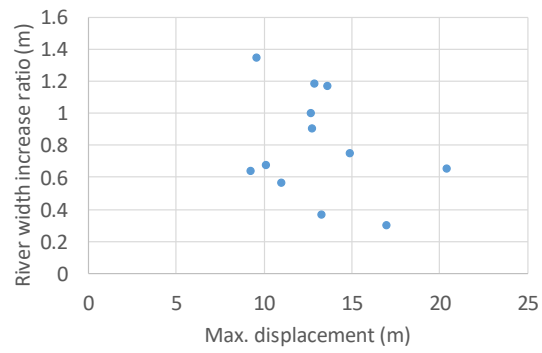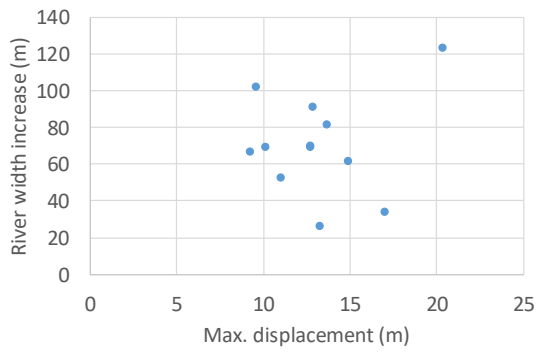
425   Google Earth Engine.

Figure A3. The relation between measured maximum slope displacements and river width increase (a) and river width increase rate (b).

Table 1. Dates of images used in the Mindu section. Image pairs with grey background are shown in Figure 3. All image pairs are used in Figure 4.

Image pairs	Reference images	Target images
#1	Jan. 03, 2017	Jan. 13, 2018
#2	Feb. 12, 2017	Apr. 03, 2018
#3	Feb. 12, 2017	Apr. 23, 2018
#4	Jan. 03, 2017	Nov. 09, 2018
#5	Jan. 03, 2017	Nov. 29, 2018
#6	Jan. 03, 2017	Dec. 09, 2018
#7	Jan. 16, 2017	Jan. 06, 2019
#8	Feb. 12, 2017	Jan. 23, 2019
#9	Feb. 12, 2017	Feb. 07, 2019
#10	Feb. 12, 2017	Mar. 14, 2019
#11	Feb. 12, 2017	Mar. 29, 2019
#12	Feb. 12, 2017	Apr. 18, 2019
#13	Jan. 03, 2017	Dec. 29, 2019
#14	Jan. 13, 2020	Jan. 13, 2020
#15	Feb. 12, 2017	Jan. 18, 2020
#16	Feb. 12, 2017	Feb. 07, 2020

435